Li, C.L. and Murray, J.W. and Voisey, K.T. and Clare, A.T. and McCartney, D.G. (2013) Amorphous layer formation in Al86.0Co7.6Ce6.4 glass-forming alloy by large-area electron beam irradiation. Applied Surface Science, 280 . pp. 431-438. ISSN 0169-4332

Amorphous layer formation in $Al_{86.0}Co_{7.6}Ce_{6.4}$ glass-forming alloy by large-area electron beam irradiation

C.L. Li[1], J.W. Murray[2], K.T. Voisey[1*], A.T. Clare[2], D.G. McCartney[1]

[1]Materials, Mechanics and Structures Research Division, Faculty of Engineering, The University of Nottingham, Nottingham NG7 2RD, UK.

[2]Precision Manufacturing Centre, Faculty of Engineering, The University of Nottingham, Nottingham NG7 2RD, UK.

Contact: C.L. Li: emxcl@nottingham.ac.uk, J.W. Murray: epxjm2@nottingham.ac.uk, K.T. Voisey (Corresponding author): katy.voisey@nottingham.ac.uk, Tel.: +44 115 951 4139; Fax: +44 115 951 3600, Postal Address: Room A30a Coates, UniversityPark, Nottingham, NG7 2RD, UK, A.T. Clare: adam.clare@nottingham.ac.uk, D.G. McCartney: graham.mccartney@nottingham.ac.uk

Abstract

Amorphous Al-Co-Ce alloys are of interest because of their resistance to corrosion, but high cooling rates are generally required to suppress the formation of crystalline phases. In this study, the surface of a bulk crystalline Al-Co-Ce alloy of a glass-forming composition was treated using large area electron beam (LAEB) irradiation. Scanning electron microscopy shows that, compared to the microstructure of the original crystalline material, the treated surface exhibits greatly improved microstructural and compositional uniformity. Glancing angle X-ray diffraction conducted on the surface of treated samples indicates the formation of the amorphous phase following 25 and 50 pulses at 35 kV cathode voltage. However, when the samples are treated with 100 and 150 pulses at 35 kV cathode voltage of electron beam irradiation, the treated layer comprises localised crystalline regions in an amorphous matrix. In addition, the formation of cracks in the treated layer is found to be localised around the Al_8Co_2Ce phase in the bulk material. Overall, crack length per unit area had no clear change with an increase in the number of pulses.

Keywords：Al-Co-Ce alloy, glass-forming, amorphous layer, electron beam irradiation

1 Introduction

Amorphous metallic alloys are capable of exhibiting better chemical properties, such as corrosion resistance, compared to the crystalline form of the same materials. This is primarily

due to the absence of grain boundaries and other defects as well as the super-saturation of alloying elements [1]. In 1960, Duwez et al. [2] first synthesized an amorphous structure in an Au-Si alloy by rapid solidification. Since then many amorphous alloys have been synthesised through various preparation techniques and their field of application has been expanded [3]. The Al-TM (transition metal) -RE (rare earth) family of amorphous alloys has been shown to be particularly promising for corrosion resistant applications [4] has attracted much attention from corrosion scientists and engineers alike. Recently, several researchers have investigated the corrosion behaviour of several Al-TM-RE amorphous alloys including Al-Fe-Gd, Al-Ni-Gd, Al-Ni-Y and Al-Co-Ce [4-6]. The critical pitting potential and pit growth behaviour of this family of amorphous alloys were shown to be improved compared to high purity, polycrystalline Al. Additionally, Jakab [7] investigated the active inhibition behaviour of Al-Co-Ce amorphous alloys and found that these alloys can inhibit corrosion by storing, releasing and delivering Co^{2+} and Ce^{3+} inhibitors.

However, Al-TM-RE alloy is difficult to produce in bulk form due to the high critical cooling rate required to achieve the amorphous phase. To date, the maximum dimension of bulk Al-based amorphous alloys achieved is a rod of about 1 mm diameter [8]. Therefore, there is interest in using surface modification techniques to generate coatings or thin films of these amorphous materials. It has been reported that Tailleart et al. [9] successfully prepared a largely amorphous Al-Co-Ce alloy coating on AA 2024 alloy by pulsed thermal spraying (PTS) and high velocity oxy-fuel spraying (HVOF) technologies using gas atomised powder as a feedstock. Kato et al. [10] also prepared an Al-Co-Y coating using mechanical milled feedstock powder on the same substrate through plasma spraying with promising corrosion resistance after salt fog testing.

The application of high-energy beam such as laser and electron beam with high cooling rates is well established as an effective method of preparing an amorphous coating or surface layer. Zr, Mg, Fe and Al [11] based amorphous alloys have all been generated through laser surface

scanning treatment on bulk materials, while Fe [12, 13], and Al [14] based amorphous alloys also have been produced by a pulsed laser process. A high-energy (0.5-1.5 MeV) scanning electron beam irradiation process has also been used to generate the amorphous phase in Zr and Cu [15] based bulk alloy. Large area pulsed electron beam (LAEB) irradiation [16] is an emerging surface modification technique. LAEB has the same advantages as other high energy beams, including high cooling rate, short process time and limited affect on the substrate. In addition, LAEB can process a large-area (60 mm diameter) with uniform intensity, thereby reducing the need for overlapping exposures and associated concerns relating to reheating and possible recrystallisation.

Over the past decade, LAEB has been applied to polish and improve the corrosion behaviour of mould surfaces [17-19], improve surface hardness in steels and magnesium alloys [20], as well as the wear resistance of Al-Si alloys [21, 22]. More relevant to the current work, Guan et al. [23] have observed localised amorphisation in a simple low-carbon steel by this process, giving evidence that the high-cooling rates associated with this technique can be applied for amorphous layer preparation. In this work, a bulk polycrystalline Al-Co-Ce alloy which falls within the compositional range of glass forming alloys previously studied by Gao et al. [24] was used as a starting material for LAEB surface treatment in order to produce and characterise the formation of an amorphous layer for the first time by this process. The aim of the present work was to investigate the potential of LAEB surface treatment to produce an amorphous layer on bulk Al-Co-Ce glass forming alloy and to characterise the microstructural changes brought about by this thermal treatment.

2. Experimental Details

2.1 Starting materials

Bulk polycrystalline Al-Co-Ce alloy used for electron beam treatment was fabricated by casting under argon atmosphere in an induction melting furnace. The composition of the as-cast material is $Al_{86.0}Co_{7.6}Ce_{6.4}$ (at. %) as determined by inductively coupled plasma optical

emission spectrometry (ICP-OES) carried out by the Sheffield Assay Office. The size of samples used for electron beam treatment was 15×15×4 mm. The surface of the as-cast material was polished using 1 μm diamond paste before electron beam treatment, producing a surface with a measure Sa of 0.13 μm. The surface roughness of the polished samples was measured by a white light Interferometer (Fogale Photomap 3D).

Before electron beam treatment, Vickers micro-hardness testing on different phases in the as-cast material was conducted using a LECO M400 micro-hardness tester. A load of 0.5 N (50 gf) and a dwell time of 15 seconds force was used. Nano-indentation testing was also performed using a Nanotest NTX (Micro. Materials Ltd.) to measure the micro-hardness in different phase in the as-cast material, with a Berkovich indenter maximum loading of 50 mN. The loading and unloading rate is10 mN/s, and the holding time at maximum loading is 60 seconds. The test was calibrated by a fused silica reference sample. The area function used in this test is as follow:

$$area = ad_p^2 + bd_p$$

where d_p is the penetration depth of the indenter, a and b are 25.958391 and 1603.233038, respectively. In both micro-hardness tests, between four and twelve usable indents were made on each phase dependent on phase size, and then the average value and standard deviation were calculated.

2.2 Large area electron beam surface treatment

A Sodick PF32A large area electron beam machine (schematic in Figure 1) was used to irradiate samples. The irradiation process is carried out in an argon and nitrogen mixture at a pressure of 0.05 Pa. The supply pressure of argon and nitrogen from the gas cylinder are 0.35 and 0.15 MPa, respectively. This inert gas mixture is used as the medium for plasma build up required for the electron generation and beam propagation. The diameter of the beam is 60 mm; with a pulse interval of 11 seconds, pulse time of 2-3 μs and energy density <10

J/cm^2. Within the 60 mm diameter, energy density is expected to be uniform [17], thereby ensuring the whole sample surface in this case is uniformly irradiated. The electron beam irradiation parameters used in this work are summarised in Table 1. Under these different treatment conditions, anode voltage and solenoid voltage are constant (5 kV and 1.5 kV, respectively), while cathode voltage and pulse number are varied.

To measure the maximum temperature the samples materials can reach during the large area electron beam irradiation, three 10×10×2 mm pure Al plates were irradiated with 50, 100 and 150 pulses of electron beam irradiation at 35 kV cathode voltage. Before irradiation, temperature labelling strip (4 level, temperature ranges of 49-65˚C, 71-88 ˚C and 93-154 ˚C, RS Components Ltd) was adhered on the back of samples, which can permanently record the maximum temperature samples reached through the colour change of temperature display area in the labelling strip. It was found the samples can reach 54 ˚C, 82 ˚C and 99 ˚C when samples were irradiated with 50, 100 and 150 pulses of electron beam, respectively, indicating that the large area electron beam process generates a progressive build up of the temperature of the bulk sample .

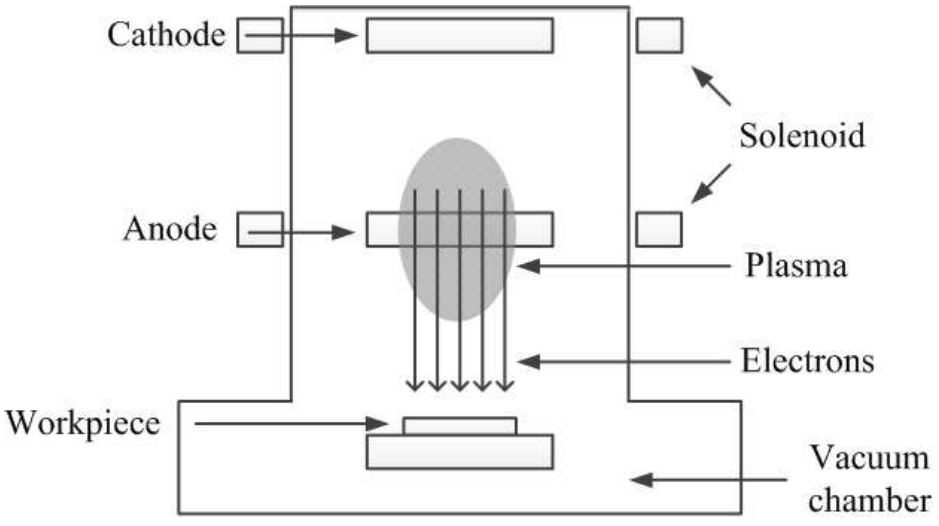

Figure 1 Schematic of LAEB irradiation process

Table 1 Large area electron beam treatment parameters

Cathode voltage (kV)	Number of pulses
15	1, 8, 15 and 25
22	1, 8, 15 and 25
29	1, 8, 15 and 25
35	1, 8, 15, 25, 50, 100 and 150

2.3 Microstructural characterisation

X-ray diffraction (XRD) was conducted before irradiation using a Siemens D500 X-ray diffractometer (Cu Kα) to examine the as-cast material. The step size used was 0.02° with a dwell time of 2 s. After electron beam irradiation, in order to analyse the outer, transformed layer in isolation, glancing angle XRD (GAXRD) was also conducted using a Bruker D8 Advance (Cu Kα) using a step interval of 0.02°, a dwell time of 8 s and an incidence angle of 2°. The surface and cross-section of treated samples were also observed using a Philips XL30 field emission gun scanning electron microscope (FEG SEM). Unless otherwise mentioned, all SEM images were taken in back-scattered mode to emphasise phase contrast. Energy dispersive X-ray spectroscopy (EDS) was used to examine the elemental composition of phases in both as-cast material and treated samples.

"Image J" image analysis software was used to measure the crack density and treated layer thickness. The total length of cracks in the treated layer was measured based on SEM images under the same magnification, and then the crack length per unit area of examined sample surface (crack density) was calculated. The thickness of treated layers was also measured from SEM images. For each crack density and treated layer thickness measurement, four SEM images with magnification of 300× and 2500× were used, respectively. In particular, the SEM images used for crack density measurement have an area of 0.626 mm^2, the minimum crack width of cracks included in these measurements was ~1.5 µm.

3 Results

3.1 Characterisation of as-cast material

The XRD pattern and microstructure of the as-cast material are shown in Figure 2 and Figure 3, respectively. Combining both EDS analysis and XRD results, it was determined that the as-cast material contained three main phases; the bright $Al_{11}Ce_3$ phase, the grey Al_8Co_2Ce phase and the dark Al-rich phase (eutectic Al and $Al_{11}Ce_3$), as shown in Figure 3. A darker edge on all grey Al_8Co_2Ce phases can also be observed. EDS analysis revealed that the darker edge contains all three Al, Co and Ce elements. It should be noted that the Al content in this phase is higher than that in Al_8Co_2Ce phase, while the ratio of Co and Ce atoms remains 2:1. A few small particles with a composition consistent with the Al_9Co_2 phase were also observed in the as-cast material. However, the above Al-Co-Ce phase and the Al_9Co_2 phase cannot be effectively distinguished although there are a few unrecognised peaks (located at 2θ of 23.3˚, 37˚, 39.2˚ and 40˚ etc.) in the XRD pattern, which is consistent with the small amount present as well as the possibility of peaks being hidden by overlapping.

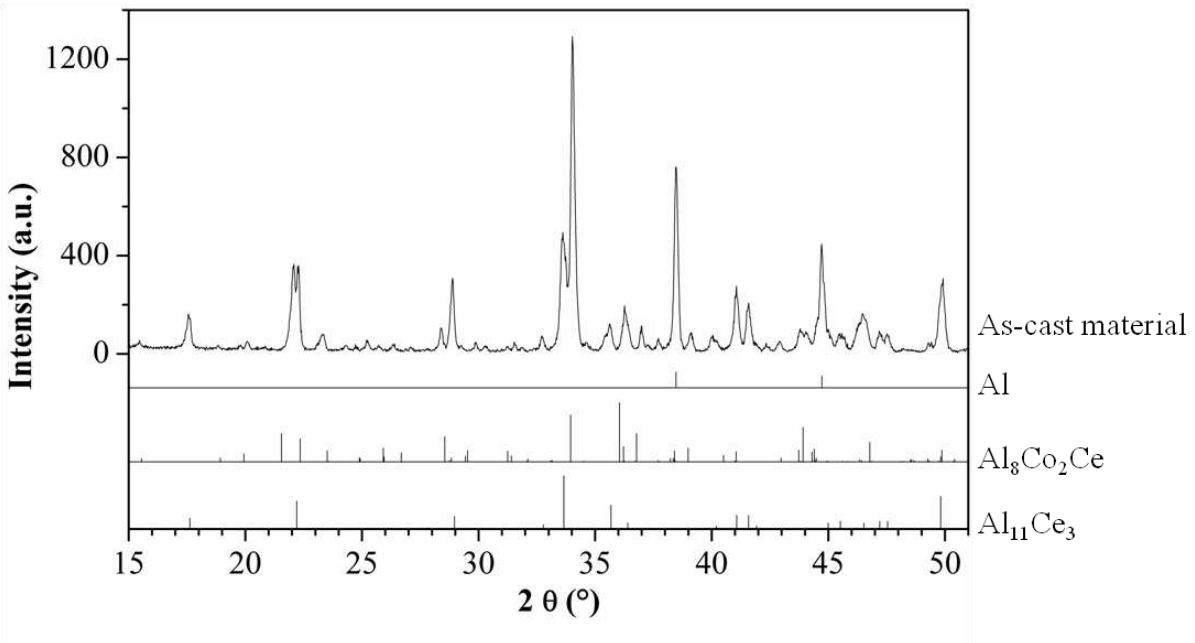

Figure 2 XRD pattern of as-cast material

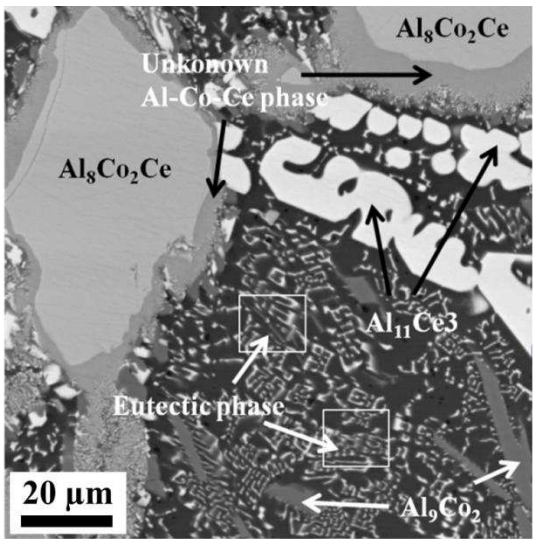

Composition (at %)	Probable phase
Al: 77.1 Ce: 22.9	$Al_{11}Ce_3$
Al: 97.4 Ce: 2.6	Al/intermetallic eutectic
Al: 72.2 Co: 18.2 Ce: 9.6	Al_8Co_2Ce
Al: 80.6 Co: 12.3 Ce: 7.0	Unknown phase
Al: 82.9 Co: 17.1	Al_9Co_2

Figure 3 Back scattered SEM micrograph and phase identification of as-cast material

The results of Vickers micro-hardness and nanoindentation testing are listed in Table 2. It can be seen that the Al_8Co_2Ce phase has the highest micro-hardness among the three main phases (743 ± 78 Hv and 9.9 ± 0.4 GPa in Vickers micro-hardness and nanoindentation hardness, respectively), while the micro-hardness of the eutectic phase is the lowest (89 ± 25 Hv and 1.0 ± 0.1 GPa in Vickers micro-hardness and nanoindentation micro-hardness, respectively). For the $Al_{11}Ce_3$ phase, Vickers micro-hardness testing did not obtain valid results due to the small phase size. However, in the nanointendention test $Al_{11}Ce_3$ phase had an intermediate micro-hardness (3.2 ± 0.3 GPa) compared with the other two phases.

Figure 4 shows a Vickers indentation in the Al_8Co_2Ce phase. It can be observed that the loading force has induced cracking within the Al_8Co_2Ce phase, initiating from a corner of the indent. In addition, there is also a crack extending from the opposite corner of the indent into the $Al_{11}Ce_3$ phase.

Table 2 Micro-hardness test results on different phases in the as-cast material

Phase type	**Eutectic phase**	**Al_8Co_2Ce**	**$Al_{11}Ce_3$**
Vickers micro-hardness (Hv)	89±25	743±78	-
Nano-indentation micro-hardness (GPa)	1.0±0.1	9.9±0.4	3.2±0.3

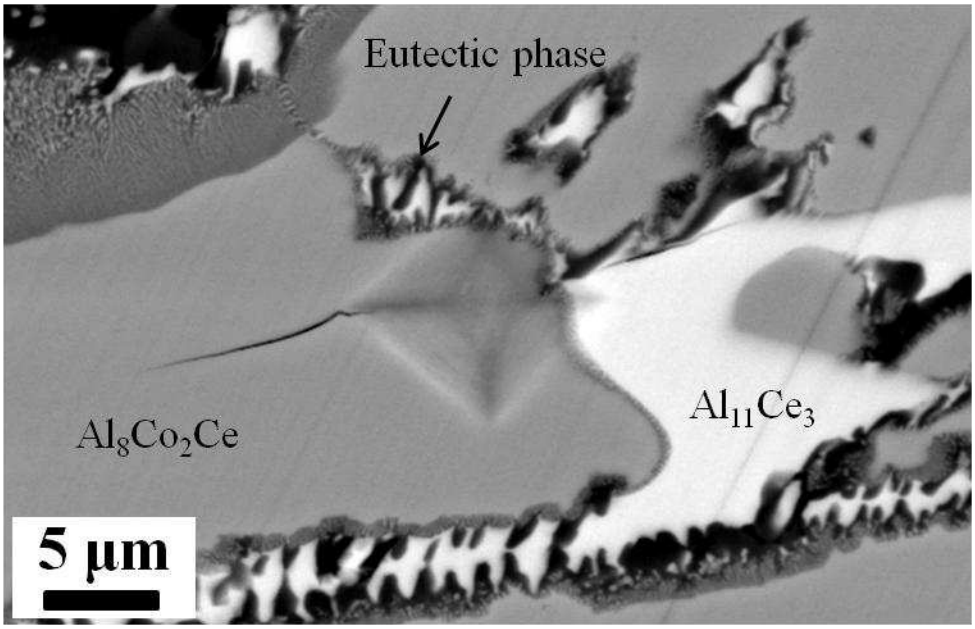

Figure 4 Crack induced by loaded force in Vickers micro-hardness test

3.2 Characterisation of LAEB treated layer

3.2.1 Surface and cross sectional morphology

Figure 5 shows the surface changes of electron beam treated samples with different treatment parameters. Overall, with increasing cathode voltage and number of pulses, the heterogeneity of as-cast materials was greatly reduced. It can also be seen that for the sample treated with 22 kV and 1 pulse, the as-cast material showed almost no change, with the three main crystalline phases retaining their original shapes, and the boundaries between them remaining defined. However, with increasing numbers of pulses, the crystalline phases experienced obvious melting and inter-phase diffusion. After treatment with 22 kV and 25 pulses, it is difficult to distinguish different phases, as mixing due to diffusion has occurred. In addition, there is an obvious decrease in the area of the dark eutectic phase in the treated sample. The 29 kV and 35 kV treated sample surfaces exhibited similar, higher levels of homogeneity with increasing number of pulses, whereas the 22 kV treated samples still retained phase structure after 25 pulses. When the material was treated with 25 pulses of electron beam irradiation at 35 kV, a relatively homogenous compositional distribution can be observed on the sample surface, as indicated by the uniformity of contrast in back-scattered imaging. Distinct phase

boundaries are not observed in the treated layer. When the sample was subject to further electron beam irradiation (35 kV and 150 pulses), a highly homogenised surface was seen, and the phase distinction of the as-cast material almost completely eliminated. It should be noted that cracking of varying severity was observed on all treated samples, and this is described further in section 3.2.3.

Cross-sections of samples irradiated at 35 kV and varying numbers of pulses are shown in Figure 6. The corresponding thicknesses of the treated layers are also plotted. It can be seen when the sample surface was irradiated with 35 kV and 1 pulse, some remelting but little diffusion occurred. Also, the remelted layer is relatively thin (2.8 µm). However, with increasing numbers of pulses, treated layer thickness had a notable increase when the sample was treated with 15 pulses of irradiation. An approximate 3 µm increase can be seen from the plot of thicknesses. In addition, the remelting of the treated layer and elemental diffusion were more noticeable. When the sample was subjected to 100 pulses of electron beam irradiation, the treated layer exhibited a straight interface with the underlying substrate. The treated layer itself also became more homogeneous in composition. Furthermore, compared to the rapid increase of treated layer thickness for samples treated with 8 pulses of irradiation, further pulses had a reduced effect in increasing the thickness of the treated layer.

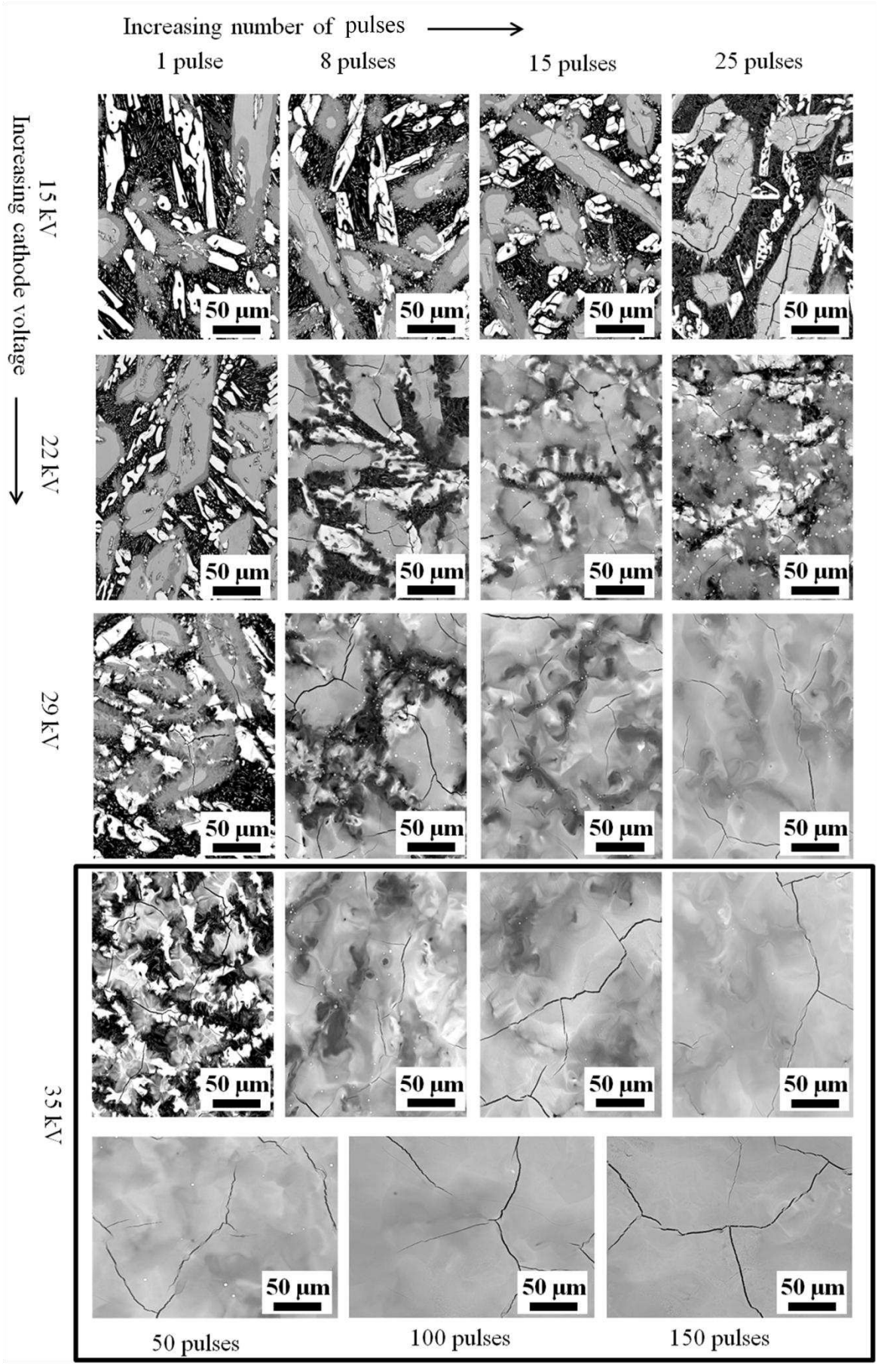

Figure 5 Surface morphology of electron beam treated sample with different cathode voltages and number of pulses.

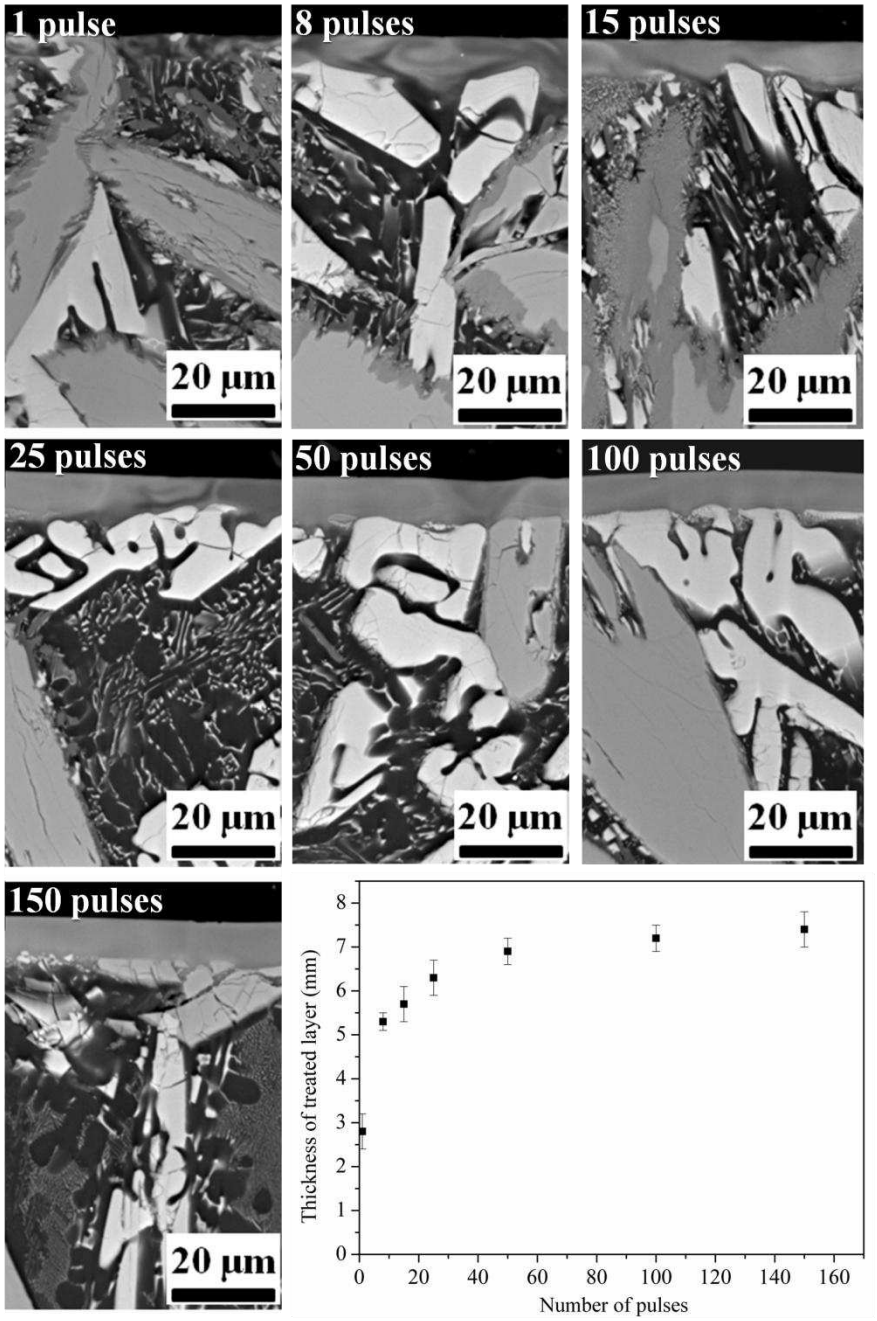

Figure 6 Cross-section morphologies of samples treated with 35 kV cathode voltage and increasing number of pulses. A plot of treated layer thickness against number of pulses is also shown.

3.2.2 Phase transformation

Figure 7 shows GAXRD patterns of electron beam treated samples which were irradiated with 35 kV and increasing numbers of pulses. Compared with the XRD result of the as-cast

material (see Figure 2) which shows a typical spectrum of a polycrystalline multi-phase material, the crystalline peak intensity in the electron beam treated samples was significantly decreased, particularly in samples treated with 35 kV and 8 or more pulses of electron beam irradiation. With increasing numbers of pulses, an obvious amorphous hump began to appear located at 38˚ (2θ) in the spectra of all treated samples. The disappearance of most of the crystalline peaks was also observed, which is consistent with a significant amorphous phase formation in the treated layer. However, several crystalline peaks with low intensity are still present in the spectra of the treated samples. It can also be noted that there was an obvious increase in the intensity of crystalline peaks when the material was treated with 100 pulses of electron beam irradiation compared to 50, 25 and 15 pulses. Particularly when the material was treated with 35 kV and 150 pulses, crystalline phase peak intensity exceeded that of the samples treated with 35 kV and 8 and 15 pulses.

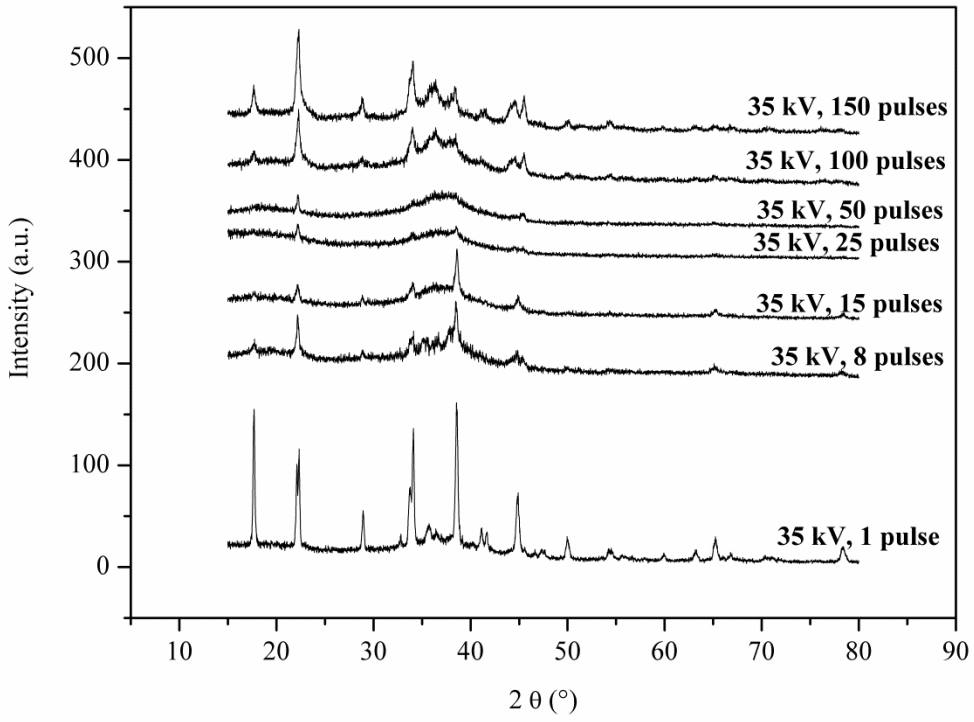

Figure 7 GAXRD patterns of electron beam treated samples (35 kV and increasing number of pulses)

Figure 8 shows crystallisation in a local area of the treated layer for the sample treated with 35 kV and 150 pulses. It can be seen that in some regions the treated layer did not exhibit uniform composition, but contained a large number of nearly spherical crystallised particles. From the magnified images (Figure 8b), the diameter of these crystals is approximately 500 nm. As well as the spherical particles, there are also a few columnar crystals with the length of 1~2 μm (Figure 8a). It should be noted that no correlation was observed between crack location and areas of crystallisation (see Figure 8c).

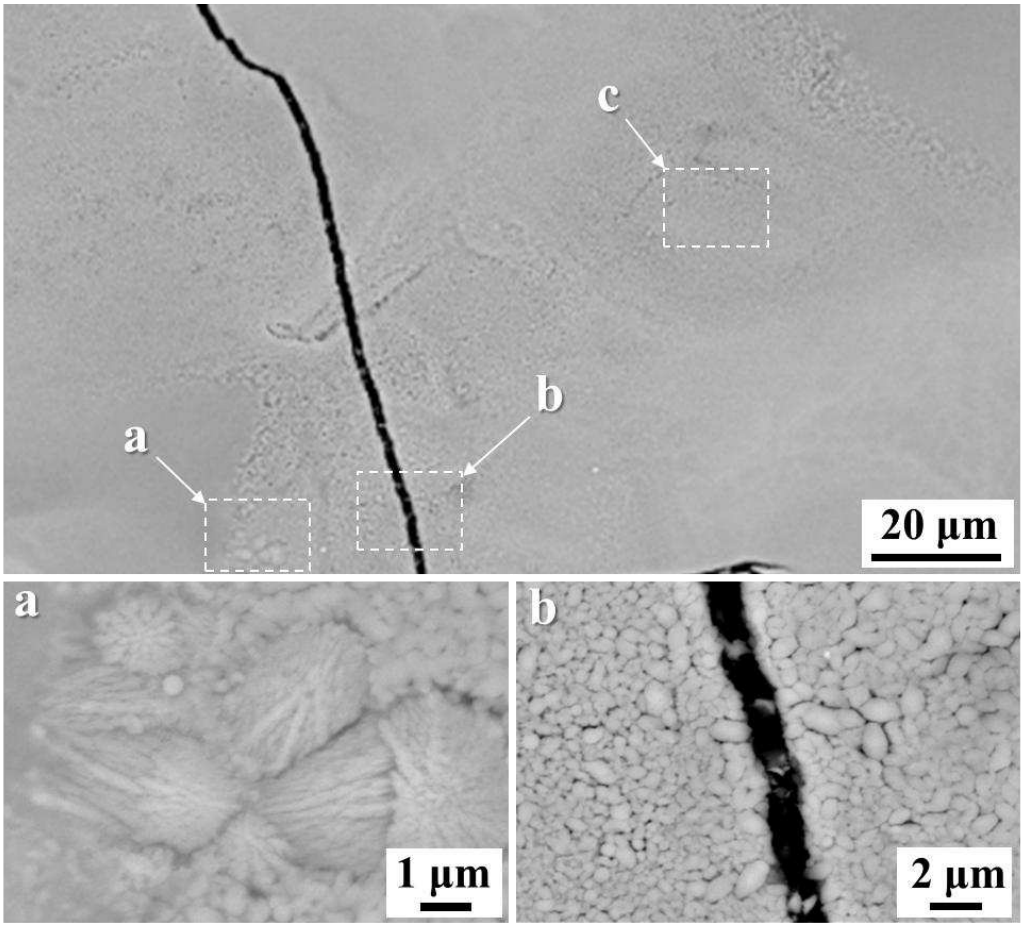

Figure 8 Localised crystallisation in the treated layer for the sample treated with 35 kV and 150 pulses, a, b and c highlight three areas in which crystallisation has occurred.

3.2.3 Cracking

Accompanied with the homogenisation of treated layer, a number of cracks appeared on almost all the treated surfaces, as shown in Figure 5. It was also observed that the cracks preferentially formed at the locations of the grey Al_8Co_2Ce phase. This is clearly seen on the

surfaces of samples which are not completely homogenised i.e. all 15 and 22 kV samples, 29 kV up to 8 pulses and the 1 pulse 35 kV sample (Figure 5). For homogenous, amorphised surfaces, cross-sectional examination again shows that the cracking is correlated with the location of underlying Al_8Co_2Ce precipitates (Figure 9a).

Observation of cracks formed on samples treated with 35 kV cathode voltage and increasing numbers of pulses was used to characterise the extent of surface cracking by the measurement and calculation of crack length per unit area (crack density). Figure 9b shows the relationship between crack density and number of pulses. Overall, crack density has no apparent change with increasing numbers of pulses. Despite this, from the surface morphologies shown in Figure 5, it can be seen that the length of individual cracks has increased, and after treatment with 35 kV and 150 pulses, cracks were observed to have joined together and formed a network.

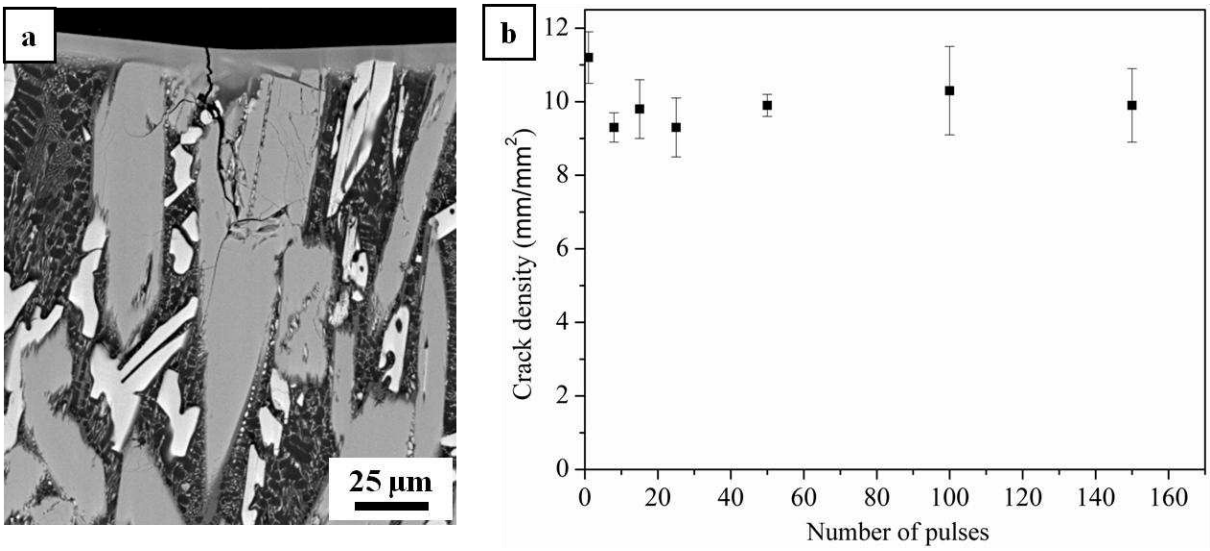

Figure 9 Cross section of the treated sample (35 kV, 150 pulses) showing a crack and crack density (crack length per unit area) against number of pulses for treatment with 35 kV cathode voltage.

4 Discussion

4.1 Homogenisation and amorphisation of the Al-Co-Ce treated layer

In the process of electron beam treatment, electrons are first accelerated by a high cathode voltage. Once these electrons impact on the surface of the original bulk material, the kinetic energy of high velocity electrons is transformed into thermal energy which quickly increases the temperature of a near surface volume. Once the temperature reaches the melting point of material, melting occurs. The new elemental distribution in the sample is then determined by the extent of flow and diffusion among the different phases. In this work, the samples treated with lower cathode voltage and fewer electron beam pulses have no apparent change in compositional homogeneity compared to the as-cast material. This can be seen from the back scattered SEM images in Figure 5 which show a similar extent of contrast, i.e. compositional variation, between different regions as was seen for the as-cast material. Furthermore, when the sample was treated with a more intense electron beam (higher cathode voltage) and higher number of pulses, the sample surface exhibited a more uniform elemental distribution due to the longer diffusion time for different phases, as shown in Figure 5. After a sufficient number of pulses at the given cathode voltage, the sample surface experienced adequate elemental diffusion to acquire a uniform composition i.e. the glass forming composition in this case.

Due to the short pulse duration (2~3 μs [17]), the melted surface will rapidly cool and solidify through heat transfer to the underlying bulk. It has been estimated that pulsed electron beam irradiation can obtain a cooling rate between 10^7 to 10^9 K/s [25-27]. Under the action of this high cooling rate, the melted liquid alloy can retain the disordered atomic arrangement i.e. the amorphous state. The results presented in this work show that a homogenous amorphous layer was achieved using a cathode voltage of 35 kV and a pulse number between 25 and 50.

4.2 Crystallisation of the Al-Co-Ce treated layer

When 100 and 150 pulses of electron beam at 35 kV were applied to the sample surface, crystalline peaks indicate that the material examined by GAXRD is not fully amorphous, but consists of some crystallisation within an amorphous matrix. The existence of spherical and columnar crystals in the treated layer (Figure 8) confirmed the GAXRD results. The occurrence of the crystallisation phenomenon with increasing pulses of irradiation may be explained by a decrease in thermal gradient between treated layer and the substrate, thereby reducing the cooling rate and permitting crystallisation as opposed to amorphous phase formation. The decrease of thermal gradient is caused from the progressive temperature increase of substrate material. As stated in the experimental methods section, temperature labelling strips applied to LAEB treated Al samples have shown that the maximum temperature reached by the back of the sample increases with number of electron beam pulses, indicating a progressive heat accumulation.

A comparison experiment was performed on the Al-Co-Ce alloy used in this work, whereby the time interval between pulses was set at 10 minutes, instead of the usual 11 seconds. After the same number of pulses and cathode voltage, samples treated with this larger pulse interval exhibited a less homogeneous compositional distribution compared to the normal pulse interval time of 11 seconds (Figure 10). This was consistent with there being some progressive heat accumulation when the shorter, 11 seconds, interval was used, allowing more time for diffusion and hence achieving the more uniform composition seen in Figure 10a.

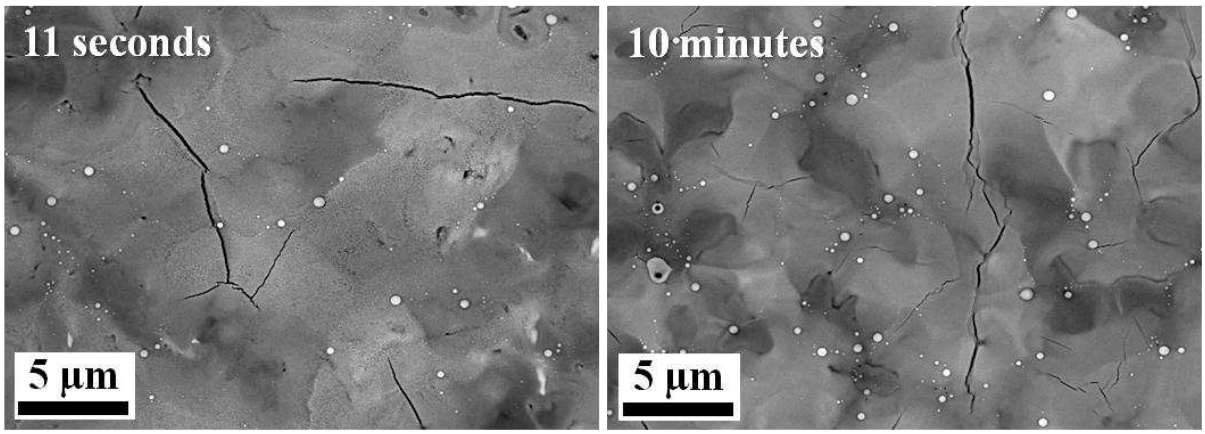

Figure 10 Surface morphologies of LAEB treated samples with different pulse intervals (40 kV, 39 pulses).

In addition, crystallisation did not occur all over the sample surface, but in some localised regions. It is thought that the appearance of localised regions of crystalline phases in the amorphous matrix may result from any remaining slight compositional heterogeneity of the treated layer. It is also possible that local variations in thermal gradients and cooling rates may arise due to the phases present in the underlying microstructure, i.e. any variation in thermal conductivity of the different phases would generate small differences in thermal history.

4.3 Cracking in the Al-Co-Ce treated layer

To accompany the phase transformation of the treated layer, cracks were also observed as a result of electron beam irradiation. Cracks were observed on all electron beam treated samples, as shown in Figure 5 and Figure 9. It is thought that there are two main causes of crack formation. Firstly, after melting of the material surface, a volume contraction is expected to occur due to the subsequent rapid cooling effect in the surface layer. However, the solid state of the substrate beneath constrains this shrinkage process and results in a tensile stress being applied to the treated layer, which results in the formation of a crack. Also, it must be noted that there are steep thermal gradients in the material, as shown by the thin treated layer. The extent of contraction due to coefficient of thermal expansion therefore varies with position,

with the top layer contracting more than the cooler underlying material. This will result in tensile stresses, with these being greatest in the top, treated layer. The cracking sites were found to correlate with the presence of a particular phase, Al_8Co_2Ce (Figure 5 and Figure 9a). This phase is brittle, as shown by crack formation under micro-hardness indentation (see Figure 4). It is proposed that, under the action of tensile stresses generated upon cooling, the Al_8Co_2Ce in the immediate vicinity of the treated layer, i.e. where the stresses are highest, will be particularly prone to crack formation, the cracks then extend through the treated layer producing the cracked surface. The cracks were also seen extended into the underlying bulk materials but constrained in the Al_8Co_2Ce phase, which is due to the brittleness characteristic of this phase. Once cracking has occurred in this phase, regional tensile stress is relieved, avoiding further cracking in other local phases. When the samples were subjected to lower cathode voltage and few electron beam pulses irradiation, it should be noted that the cracking also occurred in the $Al_{11}Ce_3$ phase. The reason was thought to be similar to that in the Al_8Co_2Ce phase. However, due to the small phase size the extent of cracking in the $Al_{11}Ce_3$ phase is not so large as that in the Al_8Co_2Ce phase. Furthermore, when higher cathode voltage and more pulses of electron beam irradiation were performed, the small cracks in this phase could easily be repaired by the elemental diffusion.

The cracking related to the existence of large and brittle Al_8Co_2Ce will clearly compromise the corrosion resistance of the amorphous layer. Our on-going work is focussed on investigating strategies to optimise the large area electron beam process in order to eliminate cracking.

5 Conclusions

- 25 - 50 pulses of 35 kV electron beam irradiation successfully transformed a 6 - 7 μm surface layer of $Al_{86.0}Co_{7.6}Ce_{6.4}$ to the amorphous state.

- Localised crystallisation of the amorphous state occurred under treatment with excessive numbers of pulses (100 and 150) at 35 kV cathode voltage, due to the decrease of cooling rate by progressive heat accumulation in the bulk sample.
- Cracks were observed to form on almost all electron beam treated samples. These were correlated with the presence of the large and brittle Al_8Co_2Ce phase.
- However, crack length per unit area had no apparent change while remelted layer thickness increased slightly with increasing numbers of pulses.

References

[1] J.R. Scully, A. Gebert, J.H. Payer, Corrosion and related mechanical properties of bulk metallic glasses, J Mater Res, 22 (2007) 302-313.

[2] W. Klement, R.H. Willens, P. Duwez, Non-crystalline structure in solidified gold-silicon alloys, Nature, 187 (1960) 869-870.

[3] A. Inoue, A. Takeuchi, Recent development and application products of bulk glassy alloys, Acta Mater, 59 (2011) 2243-2267.

[4] A.M. Lucente, J.R. Scully, Localized corrosion of Al-based amorphous-nanocrystalline alloys with solute-lean nanocrystals: Pit stabilization, J Electrochem Soc, 155 (2008) C234-C243.

[5] J.E. Sweitzer, G.J. Shiflet, J.R. Scully, Localized corrosion of $Al_{90}Fe_5Gd_5$ and $Al_{87}Ni_{8.7}Y_{4.3}$ alloys in the amorphous, nanocrystalline and crystalline states: resistance to micrometer-scale pit formation, Electrochim Acta, 48 (2003) 1223-1234.

[6] J.E. Sweitzer, J.R. Scully, R.A. Bley, J.W.P. Hsu, Nanocrystalline $Al_{87}Ni_{8.7}Y_{4.3}$ and $Al_{90}Fe_5Gd_5$ alloys that retain the localized corrosion resistance of the amorphous state, Electrochem Solid State Lett, 2 (1999) 267-270.

[7] M.A. Jakab, J.R. Scully, On-demand release of corrosion-inhibiting ions from amorphous Al-Co-Ce alloys, Nature Mater, 4 (2005) 667-670.

[8] B.J. Yang, J.H. Yao, J. Zhang, H.W. Yang, J.Q. Wang, E. Ma, Al-rich bulk metallic glasses with plasticity and ultrahigh specific strength, Scripta Mater, 61 (2009) 423-426.

[9] N. Tailleart, B. Gauthier, S. Eidelman, J.R. Scully, Metallurgical and Physical Factors Controlling the Multi-Functional Corrosion Properties of Pulsed Thermal-Sprayed Al-Co-Ce Coatings, Corrosion, 68 (2012) 035006.

[10] Y. Kato, Plasma Spraying of Aluminum-Based Glass Forming Alloys, University of Missouri-Rolla, PhD thesis, (2005)26-40.

[11] F. Audebert, R. Colaço, R. Vilar, H. Sirkin, Production of glassy metallic layers by laser surface treatment, Scripta Mater, 48 (2003) 281-286.

[12] F. Hirose, M. Takagi, H. Mori, Y. Kitoh, T. Imura, Microstructure of Fe-B-Si alloy surface layers produced by laser-quenching, Jpn J Appl Phys, 31 (1992) 3940-3945.

[13] R. Mojaver, F. Mojtahedi, H.R. Shahverdi, M.J. Torkamany, Study on feasibility of producing an amorphous surface layer of $Fe_{49}Cr_{18}Mo_7B_{16}C_4Nb_3$ by pulsed Nd:YAG laser surface melting, Appl Surf Sci, 264 (2013) 176-183.

[14] J.G. Hoekstra, S.B. Qadri, J.R. Scully, J.M. Fitz-Gerald, Laser surface modification of a crystalline Al-Co-Ce alloy for enhanced corrosion resistance, Adv Eng Mater, 7 (2005) 805-809.

[15] K. Lee, E. Yun, S. Lee, N.J. Kim, Fabrication of Zr-and Cu-base bulk metallic glass/Cu surface composites by high-energy electron-beam irradiation, Mater Sci Eng A-Struct, 408 (2005) 92-101.

[16] D. Proskurovsky, V. Rotshtein, G. Ozur, A. Markov, D. Nazarov, V. Shulov, Y.F. Ivanov, R. Buchheit, Pulsed electron-beam technology for surface modification of metallic materials, J Vac Sci Technol A, 16 (1998) 2480.

[17] Y. Uno, A. Okada, K. Uemura, P. Raharjo, T. Furukawa, K. Karato, High-efficiency finishing process for metal mold by large-area electron beam irradiation, Precis Eng, 29 (2005) 449-455.

[18] Y. Uno, A. Okada, K. Uemura, P. Raharjo, S. Sano, Z. Yu, S. Mishima, A new polishing method of metal mold with large-area electron beam irradiation, J Mater Process Technol, 187 (2007) 77-80.

[19] J.W. Murray, P. Kinnell, A. Cannon, B. Bailey, A.T. Clare, Surface finishing of intricate metal mold structures by large-area electron beam irradiation, Precis Eng, 37(2013)443-450.

[20] S. Hao, B. Gao, A. Wu, J. Zou, Y. Qin, C. Dong, J. An, Q. Guan, Surface modification of steels and magnesium alloy by high current pulsed electron beam, Nucl Instrum Meth B, 240 (2005) 646-652.

[21] Y. Hao, B. Gao, G. Tu, S. Li, S. Hao, C. Dong, Surface modification of Al–20Si alloy by high current pulsed electron beam, Appl Surf Sci, 257 (2011) 3913-3919.

[22] J. Walker, J. Murray, S. Narania, A. Clare, Dry Sliding Friction and Wear Behaviour of an Electron Beam Melted Hypereutectic Al–Si Alloy, Tribol Lett, (2011) 1-10.

[23] Q. Guan, H. Zou, G. Zou, A. Wu, S. Hao, J. Zou, Y. Qin, C. Dong, Q. Zhang, Surface nanostructure and amorphous state of a low carbon steel induced by high-current pulsed electron beam, Surf Coat Technol, 196 (2005) 145-149.

[24] M.C. Gao, N. Ünlü, M. Mihalkovic, M. Widom, G. Shiflet, Glass formation, phase equilibria, and thermodynamic assessment of the Al-Ce-Co system assisted by first-principles energy calculations, Metall Mater Trans A, 38 (2007) 2540-2551.

[25] J. Zou, Y. Qin, C. Dong, X. Wang, A. Wu, S. Hao, Numerical simulation of the thermal-mechanical process of high current pulsed electron beam treatment, J Vac Sci Technol A, 22 (2004) 545.

[26] Y. Qin, C. Dong, X. Wang, S. Hao, A. Wu, J. Zou, Y. Liu, Temperature profile and crater formation induced in high-current pulsed electron beam processing, J Vac Sci Technol A, 21 (2003) 1934-1938.

[27] D. Proskurovsky, V. Rotshtein, G. Ozur, Y.F. Ivanov, A. Markov, Physical foundations for surface treatment of materials with low energy, high current electron beams, Surf Coat Technol, 125 (2000) 49-56.

Figure Captions

Figure 1 Schematic of LAEB irradiation process

Figure 2 XRD pattern of as-cast material

Figure 3 Back scattered SEM micrograph and phase identification of as-cast material

Figure 4 Crack induced by loaded force in Vickers micro-hardness test

Figure 5 Surface morphology of electron beam treated sample with different cathode voltages and number of pulses.

Figure 6 Cross-section morphologies of samples treated with 35 kV cathode voltage and increasing number of pulses. A plot of treated layer thickness against number of pulses is also shown.

Figure 7 GAXRD patterns of electron beam treated samples (35 kV and increasing number of pulses)

Figure 8 Localised crystallisation in the treated layer for the sample treated with 35 kV and 150 pulses, a, b and c highlight three areas in which crystallisation has occurred.

Figure 9 Cross section of the treated sample (35 kV, 150 pulses) showing a crack and crack density (crack length per unit area) against number of pulses for treatment with 35 kV cathode voltage.

Figure 10 Surface morphologies of LAEB treated samples under different pulse intervals (40 kV, 39 pulses).

Table Captions

Table 1 Large area electron beam treatment parameters

Table 2 Micro-hardness test results on different phases in the as-cast material